



This work was carried out in whole or in part within the framework of the NOMATEN Center of Excellence, supported from the European Union Horizon 2020 research and innovation programme (Grant Agreement No. 857470) and from the European Regional Development Fund via the Foundation for Polish Science International Research Agenda PLUS programme (Grant No. MAB PLUS/2018/8).

This is a copy of the publication which appeared in *Acta Materialia* Volume 255, 15 August 2023, 119047, published on: 3 June 2023.

DOI: [10.1016/j.actamat.2023.119047](https://doi.org/10.1016/j.actamat.2023.119047)



Full length article



Composition stability of single fcc phase in Cr–Fe–Mn–Ni alloys: First-principles prediction and experimental validation

Mark Fedorov^a, Jan S. Wróbel^{a,*}, Witold Chromiński^{a,b}, Grzegorz Cieślak^a, Magdalena Płocińska^a, Krzysztof J. Kurzydłowski^c, Duc Nguyen-Manh^d

^a Faculty of Materials Science and Engineering, Warsaw University of Technology, ul. Wotowska 141, 02-507, Warsaw, Poland

^b NOMATEN Centre of Excellence, National Centre for Nuclear Research, ul. A. Soltana 7, 05-400, Otwock, Poland

^c Faculty of Mechanical Engineering, Białystok University of Technology, ul. Wiejska 45C, 15-351, Białystok, Poland

^d CCFE, United Kingdom Atomic Energy Authority, Abingdon, OX14 3DB, United Kingdom

ARTICLE INFO

Keywords:

High entropy alloys
Phase composition
Density functional theory (DFT)
Monte Carlo simulations
Electron backscatter diffraction (EBSD)
Calphad method

ABSTRACT

The relative phase stability of fcc and bcc Cr–Fe–Mn–Ni alloys has been investigated using a combination of density functional theory, cluster expansion (CE), and Monte Carlo (MC) simulations. The MC simulations for fcc and bcc Cr–Fe–Mn–Ni alloys performed using the CE models enabled computing the Gibbs free energies of formation of 1767 fcc and bcc alloys in the whole range of compositions of each element and analyzed as a function of temperature. In order to determine regions of stability of single fcc/bcc structures and atomic fractions of these phases in two-phase regions, we constructed the thermodynamic databases (TDBs) derived from MC simulations with their application in the OpenCalphad calculations. The results obtained using this approach are in qualitative agreement with the available experimental data from the literature and the experiments performed within this work for the samples of $[\text{CrFeMn}]_{100-x}\text{Ni}_x$ ($x = 20, 25$ and 35 at.%) alloys synthesized using arc-melting and annealed at 1273 K for 48 h. The analysis of fcc fractions of the near-equiatomic alloy compositions has enabled the identification of the alloys that are predicted to be single fcc phase for a wide range of temperatures.

1. Introduction

High entropy alloys (HEAs) are the new class of materials containing four or more components in equal or near-equal atomic percent. They have been discovered by Cantor et al. [1] and Yeh et al. [2] in the year 2004 and have been found to possess unique microstructure and properties such as high strength and excellent wear, corrosion and irradiation resistance [2–6]. For example, the yield strength and hardness of HEAs may exceed 2000 MPa [7,8] and 800 HV [9], respectively being significantly larger than in the traditional alloys.

Due to the fact that irradiation has a less detrimental effect on the properties of some HEAs in comparison with pure metals as well as conventional alloys [10–13], HEAs are considered potential candidates for applications in structural components of future fusion power plants and fission reactors of the next generation (Generation IV). In Ref. [12] it was reported that the swelling resistance of fcc Fe–Cr–Co–Mn–Ni alloy, also called Cantor alloy, under irradiation is 40 times higher than that of fcc Ni. TEM analysis showed that irradiation-induced voids in

5-component fcc HEA are significantly smaller than in pure Ni and FeNi alloy.

Unfortunately, the application of Cantor alloy in fission and fusion power plants is restricted due to the presence of cobalt, which activates under irradiation. This motivated design and development of Co-free fcc HEA for nuclear applications, one of them being Cr–Fe–Mn–Ni. As it was shown in Ref. [10], the radiation-induced segregation in this HEA is much suppressed as compared with the Fe–Cr–Ni and Fe–Cr–Mn austenitic alloys. However, choosing optimal compositions of Fe, Cr, Mn and Ni is not straightforward. Since Cr is a bcc stabilizer, Ni is an fcc stabilizer, the ground state of Mn is the complex alpha structure, and Fe can possess either the bcc or fcc structure depending on the temperature, it is difficult to predict the region of stability of fcc alloys in Cr–Fe–Mn–Ni system. Moreover, as it was presented in our previous work [14], the formation of intermetallic phases might take place in a wide range of compositions at lower temperatures, i.e. below ~1200 K in the near-equiatomic region.

* Corresponding author.

E-mail addresses: mark.fedorov@pw.edu.pl (M. Fedorov), jan.wrobel@pw.edu.pl (J.S. Wróbel), witold.chrominski@pw.edu.pl (W. Chromiński), grzegorz.cieslak@pw.edu.pl (G. Cieślak), magdalena.plocinska@pw.edu.pl (M. Płocińska), k.kurzydowski@pb.edu.pl (K.J. Kurzydłowski), duc.nguyen@ukaea.uk (D. Nguyen-Manh).

<https://doi.org/10.1016/j.actamat.2023.119047>

Received 30 June 2022; Received in revised form 25 May 2023; Accepted 30 May 2023

Available online 3 June 2023

1359-6454/Crown Copyright © 2023 Published by Elsevier Ltd on behalf of Acta Materialia Inc. This is an open access article under the Open Government License (OGL) (<http://www.nationalarchives.gov.uk/doc/open-government-licence/version/3/>).

The experimental studies on HEA Cr–Fe–Mn–Ni alloys [10,15–27] showed the complexity of the respective phase diagrams. The equiatomic alloy decomposes into the fcc and bcc phases [18,19,24,26]. A similar decomposition was also observed in Cr_xFeMnNi ($x = 0.8, 1.0, 1.2, 1.5$) [26] whereas in $\text{Cr}_{24}\text{Fe}_{40}\text{Mn}_{28}\text{Ni}_8$ alloy [23] presence of sigma (σ) phase was reported. A few compositions characterized by single fcc-phase alloys, including $\text{Cr}_{18}\text{Fe}_{28}\text{Mn}_{26}\text{Ni}_{28}$, were indicated in [10,15,17,20–23,25–27]. Single fcc phase $\text{Cr}_{18}\text{Fe}_{28}\text{Mn}_{26}\text{Ni}_{28}$ alloy was investigated by scientists from Oak Ridge National Laboratory (ORNL) that exhibited excellent radiation-resistant properties [10]. The single fcc phase for the ORNL alloy was confirmed in Refs. [20,25]. The presence of Cr-rich bcc precipitates in the alloy with the same composition as the ORNL, both in the sample annealed at 1173 K and in the ion irradiated sample, was reported in Ref. [16]. The decomposition under ion irradiation was also observed for the alloy with similar composition, $\text{Cr}_{18}\text{Fe}_{29}\text{Mn}_{23}\text{Ni}_{30}$ with MnNi precipitates formed.

Phase stability of Cr–Fe–Mn–Ni was investigated theoretically using the DFT-based MC simulations [14], MD simulations [28] and CALPHAD method [15,21,27]. In order to investigate chemical ordering and the formation of ordered intermetallic phases in fcc Cr–Fe–Mn–Ni alloys, we developed in our previous work [14] a model combining the density functional theory (DFT) and cluster expansion (CE) method with Monte Carlo (MC) simulations.

The MC simulations performed using the CE model have shown, among others, that for a wide range of compositions of Cr–Fe–Mn–Ni alloys, there is a strong tendency to form the ordered intermetallic L1_0 MnNi phase. We found that this phase is expected to be present also in ORNL alloy. This agrees well with the fact that this phase was found experimentally in an irradiated alloy with a composition similar to the ORNL [17]. In the previous paper, we also demonstrated that the stability of solid solutions could be increased by a decrease in the concentration of Ni in comparison with the equiatomic composition [14].

Enthalpies of mixing of the fcc alloys in the Cr–Fe–Mn–Ni system and its subsystems were provided in [28] using the interatomic potential developed with the embedded atomic method. Minimum and maximum values for the cohesive energy difference between the fcc and bcc phases were also reported. However, the regions of stability of fcc and bcc alloys have not been studied.

CALPHAD method was applied to investigate the phase stability as a function of temperature for some compositions in [15,21,27,29,30]. In Ref. [21], phase diagrams for all ternary subsystems and iso-chromium section of the Cr–Fe–Mn–Ni at a constant content of 20 at. % Cr at 1373 K have been reported.

In general, the CALPHAD method is very useful for the prediction of phase stability of alloys, however, due to a limited number of thermodynamic data for alloys within the Cr–Fe–Mn–Ni system, the databases applied in the CALPHAD method for HEA compositions are not readily available. To overcome this issue, a thermodynamic database may be developed from first principles.

In this work, in order to investigate the stability of fcc and bcc structures, we have developed the DFT-based CE model for the bcc Cr–Fe–Mn–Ni system. One of our goals was to compare the results of MC simulations for bcc alloys with those presented in Ref. [14] for fcc alloys. The regions of stability of fcc and bcc phases and the coexistence of both phases as well as their fractions in Cr–Fe–Mn–Ni alloys have been investigated using the method, where in order to take advantage of CALPHAD, we have developed thermodynamic databases for the Cr–Fe–Mn–Ni system derived from MC simulations, and we have used them in the OpenCalphad calculations [31].

This paper is structured as follows. A section on methodology (Section 2) presents a short overview of the constructed models (Section 2.1) and the methodology we used to calculate the phase composition using models for fcc and bcc lattices (Section 2.2), as well as computational details (Section 2.3) and experimental methods (Section 2.4) used in this work.

Phase stability at 0 K, as obtained from DFT calculations, is described in Section 3. Finite-temperature phase stability, as obtained from OpenCalphad calculations using TDBs fitted on DFT-based MC simulations, is presented in Section 4, where we first analyze the difference between Gibbs free energies of formation for fcc and bcc lattices (Section 4.1), then we find a region of coexistence of fcc and bcc and quantify it (Section 4.2), and finally illustrate the effect of each element on the relative phase stability (Section 4.3).

Validation of our model is presented in Section 5, in which our theoretical results are compared with data available from the literature (Section 5.1), and with our experimental results (Section 5.2). Lastly, we present in Section 6 a number of near-equiatomic compositions that are potentially single fcc phases. Conclusions are given in Section 7.

2. Methodology

2.1. DFT-based Cluster Expansion method and Monte Carlo simulations for multicomponent systems

A detailed description of the methodology can be found in the previous works of the authors [14,32–34] and in the references therein. This work builds upon Ref. [14] on fcc Cr–Fe–Mn–Ni, adding into consideration a model for bcc Cr–Fe–Mn–Ni and subsequently studying the relative stability of Cr–Fe–Mn–Ni alloys with those lattices.

First, we calculate the mixing enthalpies, H_{mix} , of a set of structures that comprises the whole composition range of the investigated system, where each structure is described by a set of configuration variables $\vec{\sigma}$:

$$H_{mix}^{DFT}(\vec{\sigma}) = E_{tot}^{lat}(\vec{\sigma}) - \sum_{p=1}^K c_p E_{tot}^{lat}(p), \quad (1)$$

where K is the number of alloy components and c_p are the average concentrations of p 'th alloy component. In this work, we calculated mixing enthalpies from the Density Functional Theory (DFT) calculations with full relaxation and including collinear magnetism.

Then, we map the calculated H_{mix}^{DFT} to the simple-lattice-based Cluster Expansion model, where H_{mix}^{CE} are calculated as follows:

$$H_{mix}^{CE}(\vec{\sigma}) = \sum_{\omega,n,s} J_{\omega,n}^{(s)} m_{\omega,n}^{(s)} \langle \Gamma_{\omega,n}^{(s')}(\vec{\sigma}) \rangle_{\omega,n,s}, \quad (2)$$

where the summation is performed over all the clusters, distinct under symmetry operations in the studied lattice, represented by the following parameters: ω and n are the cluster size (the number of lattice points in the cluster) and its label (related to maximal distance between two atoms in the cluster), respectively; (s) is the decoration of cluster by point function $\gamma_{j,K}(\sigma_i)$; $m_{\omega,n}^{(s)}$ denotes the site multiplicity of the decorated clusters (in per-lattice-site units); and $J_{\omega,n}^{(s)}$ represents the Effective Cluster Interaction (ECI) energy corresponding to the same (s) decorated cluster.

$\langle \Gamma_{\omega,n}^{(s')}(\vec{\sigma}) \rangle_{\omega,n,s}$ are the cluster functions, averaged over all the clusters of size ω' and label n' decorated by the sequence of point functions (s') that are equivalent by the symmetry to the cluster ω, n and decorated by the same sequence of point functions (s) . Later in the text, $\langle \Gamma_{\omega,n}^{(s')}(\vec{\sigma}) \rangle_{\omega,n,s}$ is referred to as $\langle \Gamma_{\omega,n}^{(s)}(\vec{\sigma}) \rangle$ for ease of notation. In Monte Carlo formalism, cluster functions are also averaged over all MC steps at a chosen temperature, which controls the accuracy and the computational costs of the calculations.

The definition of point functions in this work is the same as in Ref. [35] and as following:

$$\gamma_{j,K}(\sigma_i) = \begin{cases} 1 & \text{if } j = 0, \\ -\cos\left(2\pi\left[\frac{j}{2}\right]\frac{\sigma_i}{K}\right) & \text{if } j > 0 \text{ and odd,} \\ -\sin\left(2\pi\left[\frac{j}{2}\right]\frac{\sigma_i}{K}\right) & \text{if } j > 0 \text{ and even,} \end{cases} \quad (3)$$

where $i = 0, 1, 2, \dots, (K - 1)$, j is the index of point functions $j = 0, 1, 2, \dots, (K - 1)$ and $\left[\frac{j}{2}\right]$ stands for the ceiling function – rounding up to the closest integer.

The cluster function is then defined as the product of orthonormal point functions of occupation variables [36] $\gamma_{j,K}(\sigma_j)$, on specific cluster described by ω and n :

$$\Gamma_{\omega,n}^{(s)}(\vec{\omega}) = \gamma_{j_1 K}(\sigma_{j_1}) \gamma_{j_2 K}(\sigma_{j_2}) \cdots \gamma_{j_{\omega} K}(\sigma_{j_{\omega}}). \quad (4)$$

Using the Structure Inversion Method, the optimal values of ECIs are found that minimize the Cross-Validation Score between H_{mix}^{DFT} and H_{mix}^{CE} :

$$CVS^2 = \frac{1}{N} \sum_{i=1}^N (E_{DFT}^i - E_{CE}^i)^2, \quad (5)$$

where E_{CE}^i is the energy of the i th structure, predicted by fitting CE energies to DFT energies, excluding E_{DFT}^i of the i th structure.

ECIs are used to parameterize Monte Carlo simulations, enabling us to calculate Gibbs free energy of formation at finite temperatures.

Since we are interested in comparing the phase stability of two different lattices, we cannot compare H_{mix} , which is calculated with respect to different ground states for each lattice. Instead, we need to compare the formation enthalpies, H_{form} , which can be calculated similarly to Eq. (1), but with respect to the global ground states (GS) of each element:

$$H_{form}^{DFT}(\vec{\sigma}) = E_{tot}^{lat}(\vec{\sigma}) - \sum_{p=1}^K c_p E_{tot}^{GS}(p), \quad (6)$$

where K is the number of alloy components and c_p are the average concentrations of p 'th alloy component.

In the present study within the Cluster Expansion framework, H_{form} for fcc and bcc alloys can be obtained from H_{mix} by including the correction coming from each element:

$$H_{form}^{CE}(\vec{\sigma}) = H_{mix}^{CE,lat} + \sum_{p=1}^K c_p (E_{tot}^{lat}(p) - E_{tot}^{GS}(p)), \quad (7)$$

where $H_{mix}^{CE,lat}$ is calculated for each lattice using Eq. (2); $E_{tot}^{lat}(p)$ and $E_{tot}^{GS}(p)$ are the reference energies of p 'th element in chosen lattice and p 'th element in a true GS, respectively, calculated using DFT; K is the number of alloy components and c_p are the average concentrations of p 'th alloy component.

At finite temperatures, entropy plays an important role in the stability of alloys. In this paper, we focus mainly on configurational entropy as the strongest entropic contribution to the Gibbs free energy of formation [36,37].

With formation enthalpies and configurational entropies considered, the Gibbs free energy of formation, G_{form} , can be calculated by applying MC simulations using the CE models for each lattice:

$$G_{form}^{CE,lat}(\vec{\sigma}, T) = H_{form}^{CE,lat}(\vec{\sigma}, T) - T S_{conf}^{lat}(\vec{\sigma}, T), \quad (8)$$

which is used to estimate the relative phase stability at finite temperatures.

The most exact way to calculate configurational entropy during Monte Carlo simulations based on Cluster Expansion's ECI is by using the thermodynamic integration (TDI) method [32,38,39]. Within TDI, configurational entropy is calculated as follows:

$$S_{conf}^{TDI,lat}(\vec{\sigma}, T) = \int_0^T \frac{C_{conf}^{lat}(\vec{\sigma}, T')}{T'} dT', \quad (9)$$

where $C_{conf}^{lat}(\vec{\sigma}, T')$ is the configurational contribution to the specific heat, which is related to the fluctuations of the mixing enthalpy in MC simulations at each temperature T' :

$$C_{conf}^{lat}(\vec{\sigma}, T) = \frac{\langle H_{mix}^2(\vec{\sigma}, T) \rangle - \langle H_{mix}(\vec{\sigma}, T) \rangle^2}{T^2}, \quad (10)$$

where $\langle H_{mix}(\vec{\sigma}, T) \rangle$ and $\langle H_{mix}^2(\vec{\sigma}, T) \rangle$ are the mean and mean squared enthalpies of mixing, respectively, meaning that the numerator describes the variance of $H_{mix}(T)$.

Formulation of configurational entropy using TDI is sound and should produce, in theory, the most exact values of $S_{conf}^{lat}(\vec{\sigma}, T)$. In reality, it is sensitive to the number of MC steps in the accumulation stage at each temperature, which affects the variance of $H_{mix}(T)$, and the temperature step of the simulations, which affects the integration in Eq. (9). The transitions related to the atomic ordering in the alloy affect configurational entropy in the TDI method since they result in the diverged values of $C_{conf}^{lat}(\vec{\sigma}, T')$ in the form of sharp narrow peaks [32,34]. Integrating over those peaks using Eq. (9) results in the discontinuous shape of the entropy curve $S_{conf}^{lat}(\vec{\sigma}, T)$ and the value of the jump may be subject to error due to the inaccuracy of the integration, as discussed in Ref. [34]. Consequently, the configurational entropy values computed using TDI at the high-temperature limit may deviate from the ideal entropy. Additionally to this issue, in view of the aim of the current work, the TDI method is unreasonably time-consuming, and as such, an approximation for configurational entropy is required. One such approximation that only requires the final configuration of MC simulations and, as such, can be applied for arbitrarily large temperature steps is the Bethe–Guggenheim quasichemical approximation [40,41]. Within this approximation, entropy can be expressed through concentrations c_i of the elements and pair probability functions of first nearest neighbors (1NN), $y_{2,1}^{ij}(\vec{\sigma}, T)$.

For the fcc system, it is expressed as follows:

$$S_{conf}^{1NN, fcc}(\vec{\sigma}, T) = 11 \sum_i c_i \ln c_i - 6 \sum_{ij} y_{2,1}^{ij} \ln y_{2,1}^{ij}, \quad (11)$$

which has been used in Ref. [14].

For the bcc system, it is expressed as:

$$S_{conf}^{1NN, bcc}(\vec{\sigma}, T) = 7 \sum_i c_i \ln c_i - 4 \sum_{ij} y_{2,1}^{ij} \ln y_{2,1}^{ij}, \quad (12)$$

which has been applied in Ref. [33].

This method reproduces the values of ideal configurational entropy in the high-temperature limit but can underestimate entropy below order–disorder transition temperatures and can even yield negative values of entropy at low temperatures. This issue is discussed more in Section 4.1.

Finally, it should be stressed once again that in this work, we focus mainly on the configurational entropy since its contribution to the Gibbs free energy of formation and its influence on the stability of alloys is notably bigger in comparison with the contributions of vibrational, electronic and magnetic entropies of mixing, as it was discussed in Refs. [14,37]. The magnetic and vibrational contributions to G_{form} are taken into account in the form of correction coming from Fe, for which the magnetic and vibrational effects are the most significant. We applied the correction to the fcc–bcc G_{form} difference from Ref. [42], which stabilizes the fcc phase of Fe over the bcc phase in the temperature range between 1315 K and 1795 K and enables to reproduce the high-temperature γ -loop in Fe. Importantly, the correction was derived in Ref. [42] from MC simulations using the magnetic CE model based on DFT calculations, which means that it is consistent with the DFT-based models applied in this work. In Ref. [32], the correction was extended into the Cr–Fe–Ni system, assuming that it is proportional to the concentration of Fe in the considered alloy. In a similar way, it is applied in this work for Cr–Fe–Mn–Ni alloys.

2.2. Phase composition for multicomponent systems

The investigation of phase composition based on the Gibbs free energies of formation of alloys from MC simulations is quite straightforward in the case of binary alloys. First of all, in the case of a two-phase mixture, it is possible to predict which phase is more stable by analyzing curves of Gibbs free energies of formation for both phases. Moreover, the regions of stability of phase 1 and phase 2, as well as the region of coexistence of both phases, are determined by the equality of the chemical potential for each phase, which is derived by

an application of the common tangent construction procedure. Then, by using the subsequent lever rule calculation, it is possible to compute the fractions of the considered phases as functions of concentration. In the case of multicomponent fcc and bcc Cr–Fe–Mn–Ni alloys, the phase composition is also determined by the equality of the chemical potential of fcc and bcc phases. However, the calculation of fractions of both phases in a 4-dimensional composition space cannot be achieved by the application of one common tangent. A well-established CALPHAD method [43] provides algorithms for calculating multi-component equilibria [44] necessary for assessing the corresponding phase fractions. In this work, we developed our own thermodynamic databases derived from our MC simulations and applied the CALPHAD method to compute phase fractions in a multi-component multi-phase Cr–Fe–Mn–Ni system.

2.2.1. Development of thermodynamic databases based on MC simulations and OpenCalphad calculations

The CALPHAD method is implemented in various licensed and free software such as Thermo-Calc [45], Pandat [46], OpenCalphad [31], etc. The input on which such software operates is a thermodynamic database that has an analytical description of partial Gibbs free energies for all elements and phases present in the investigated system, put together in one thermodynamic database (TDB) file. The analytical equations for Gibbs free energy of formation have the following general form [43]:

$$G_{form} = G_{ref} + G_{ideal} + G_{xs}, \quad (13)$$

where G_{ref} is the reference energy of the elements present in the alloy, $G_{ideal} = -TS_{ideal}$ is the contribution from the ideal configurational entropy of mixing, and G_{xs} is the excess Gibbs free energy of formation due to non-ideal interaction between the components of the alloy.

Such analytical equations for partial Gibbs free energies are usually fitted based on existing data from experiments or calculations. Since our goal is to predict the stability of a single fcc phase from first principles, instead of utilizing existing hybrid databases, based on both experimental and theoretical data, we decided to create TDB based only on the results of MC simulations obtained using the DFT-based CE models for fcc and bcc Cr–Fe–Mn–Ni alloys, described in Section 2.1.

In order to include configurational entropy coming from pair interactions, it should be included in the excess term. In such a case, also taking into account that the output of the MC simulations is the formation enthalpy ($H_{form}^{MC,lat}$), the G_{xs} from our MC simulations, which will be used for fitting, can be written as follows:

$$G_{xs}^{MC,lat}(\vec{\sigma}, T) = H_{form}^{MC,lat}(\vec{\sigma}, T) - G_{ref}^{MC} - T(S_{conf}^{lat} - S_{ideal}). \quad (14)$$

In this work, TDBs for fcc and bcc Cr–Fe–Mn–Ni alloys are developed by using a sqs2tdb tool [47] provided in the ATAT software package. The sqs2tdb code is originally designed to fit excess Gibbs free energies of formation, G_{xs} , based on the DFT calculations for special quasi-random structures (SQSs). However, in principle, it can also be used for fitting the results of MC simulations, assuming that the available polynomial terms can correctly reproduce the energy landscape obtained from MC simulations. Fitting of the excess Gibbs free energies of formation is performed using Legendre's polynomials of second order. The contribution of non-ideal binary interactions to G_{form} is described using second-order polynomials:

$$G_{xs}^{binary} = \sum_{i=0}^L G_{AB,i} X_A X_B (X_B - X_A)^i, \quad (15)$$

and the contribution of ternary interactions is described using the third-order polynomial:

$$G_{xs}^{ternary} = G_{ABC} X_A X_B X_C (V_A X_A + V_B X_B + V_C X_C), \quad (16)$$

where $V_i = X_i + (1 - X_A - X_B - X_C)/3$, and X_A , X_B and X_C are the concentrations of considered elements A, B and C, respectively. In the final version of TDB for fcc and bcc Cr–Fe–Mn–Ni alloys, the series of

binary interactions are truncated at three polynomial terms ($L = 3$ in Eq. (15)) since such fitting produced a least RMS error. sqs2tdb fitting has been attempted including quaternary interactions (G_{ABCD}), however, the fitted models consistently produced $G_{ABCD} = 0$ for quaternary interactions, meaning that they would not be contributing to the description of the Gibbs free energies of the phases. As such, quaternary interactions are not present in the final TDB. Due to its original intent, sqs2tdb can only fit energies at one temperature. The energy landscape, however, changes with temperature, and cannot be represented by only one set of polynomials. In the intended use-case of sqs2tdb, the temperature dependency of G_{form} is contained in the G_{ref} supplied from the existing databases, such as SGTE [48], which contradicts our desire of developing the TDB from the first principles. Therefore, we create a number of TDBs for all temperatures investigated using MC simulations and calculate phase equilibria using OpenCalphad code [31] at each temperature using respective TDBs. Thermodynamic databases developed within this work are available on request.

Finally, it has to be stressed once again that our work aims to predict the phase stability of fcc and bcc Cr–Fe–Mn–Ni alloys from the first principles. Thus, the data from the SGTE database [48] has not been used in our model. In particular, in order to be consistent with the DFT results, instead of empirical magnetic models used in the SGTE database, we have applied the magnetic and vibrational correction to the fcc-bcc G_{form} difference for pure Fe from Ref. [42], which was derived from MC simulations using the DFT-based magnetic CE model. As described in Section 2.1, the value of correction is proportional to the concentration of Fe in the considered alloy.

2.3. Computational details

The ready model for fcc Cr–Fe–Mn–Ni has been taken from Ref. [14], and the model for bcc has been created in a similar way as described therein, and in Refs. [32,33,49].

DFT calculations with collinear spin-polarization were performed using the projector augmented wave (PAW) method implemented in VASP [50–55]. Exchange and correlation were treated in the generalized gradient approximation GGA-PBE [56]. The electron configurations of Fe, Cr, Mn and Ni in PAW potentials were [Ar]3d⁷4s¹, [Ar]3d⁵4s¹, [Ar]3d⁶4s¹ and [Ar]3d⁹4s¹, respectively.

Total energies were calculated using the Monkhorst–Pack mesh [57] of k-points in the Brillouin zone, with the k-mesh spacing of 0.2 Å⁻¹. This corresponds to 12 × 12 × 12 k-point mesh for a four-atom fcc conventional unit cell or 14 × 14 × 14 k-point mesh for a bcc conventional unit cell. The plane wave cut-off energy used in the calculations was 400 eV. The total energy convergence criterion was set to 10⁻⁶ eV/cell, and force components were relaxed to 10⁻⁴ eV/Å.

Mapping DFT energies to CE was performed using the ATAT package [35,58–60]. As described in Ref. [14], for the fcc system, mapping of the mixing enthalpies of 835 structures (including binary, ternary and quaternary) was performed to achieve the cross-validation score of 13 meV. The set of clusters, which have minimized the CVS, consists of 6 two-body, 2 three-body and 1 four-body undecorated clusters.

For the bcc system, the final database consisted of 1062 structures (including binary, ternary and quaternary), and the CVS is equal to 19 meV. The set of clusters, which have minimized the CVS, consists of 8 two-body, 1 three-body and 1 four-body undecorated clusters.

Compositions, for which DFT calculations were performed and later used in the CE model are illustrated in the Supplementary Material, Fig S1. Size ω , label n , decoration (s), multiplicity $m_{\omega,n}^{(s)}$, coordinates of points and Effective Cluster Interactions $J_{\omega,n}^{(s)}$ (in meV) of aforementioned clusters for bcc system are listed in the Supplementary Material, Tables S1–S2 and Fig. S2. Effective cluster interactions for fcc Cr–Fe–Mn–Ni have been taken from our previous model and can be found in Table I in Ref. [14].

Canonical MC simulations were also performed using the ATAT package separately for fcc and bcc lattices, containing 2048 atoms in the form of $8 \times 8 \times 8$ fcc unit cells and 2000 atoms in the form of $10 \times 10 \times 10$ bcc unit cells, respectively. For each composition, simulations were performed starting from a disordered high-temperature state at $T = 3000$ K. The alloy was then cooled down with the temperature step of $\Delta T = 100$ K, with 2000 equilibration and accumulation Monte Carlo passes. The aforementioned CVS can be converted into the errors of MC simulations, being equal to 150 K and 220 K for fcc and bcc models, respectively.

2.4. Experimental methods

Samples of three pseudobinary alloys $[\text{CrFeMn}]_{100-x}\text{Ni}_x$ with three different Ni concentrations, $x = 20, 25$ and 35 at.%, and with other elements kept equiatomic, were obtained by using arc-melting under an argon atmosphere of elemental powders (Fe — Alfa Aesar 99.99% purity, Ni — Sigma Aldrich 99.95%, Mn — Sigma Aldrich 99.95%, and Cr — Alfa Aesar 99.99%). Each ingot, of approximately 15 g mass, was re-melted at least three times to assure higher homogeneity of chemical composition.

As cast samples were finally annealed at 1273 K for 48 h followed by water quenching. Microstructure and phase composition of as-cast and annealed samples were characterized using electron backscatter diffraction (EBSD) and scanning electron microscopy (SEM) combined with energy dispersive X-ray spectroscopy (EDS).

Samples for SEM observations were prepared with conventional grinding with decreasing sand paper gradation and polishing mechanically to a mirror-like surface. Directly before observations, samples were gently cleaned with a low-energy argon plasma to enhance the signal-to-noise ratio.

Microstructural observations were carried out with a Hitachi SU70 analytical scanning electron microscope equipped with a field emission gun. EBSD maps were collected using Bruker e-flash HD detector. EBSD data post-processing was carried out with Channel 5 software. EDS data processing was performed in Thermo Scientific's dedicated software. Quantification of data was performed with standard procedures.

3. Zero-temperature properties

Formation enthalpies for fcc and bcc binary systems computed using DFT at 0 K are presented in Fig. 1. Among six binary systems, only in the Fe–Cr system are the bcc structures more stable than the fcc structures for the whole range of compositions. As shown in Fig. 1(a), there exist structures with slightly negative formation enthalpies in the Fe-rich region that were reported in the previous works [32,61,62]. There is also only one binary system, Mn–Ni, in which fcc phases are more stable for all compositions (see Fig. 1(f)). It should be noted that the $L1_0$ MnNi structure is the most stable intermetallic phase in the Cr–Fe–Mn–Ni system. For the remaining four binary systems, the convex hulls for the fcc and bcc structures intersect, meaning that there exists a region where the fcc phase should be more stable than the bcc phase and *vice versa*. In practice, in all of those systems, there exist regions of possible coexistence of the fcc and bcc phases, which are indicated in Fig. 1(b)–(e) by black dashed lines. The regions of coexistence of bcc and fcc at 0 K with negative formation enthalpies are observed for two systems, where ground states are fcc for one element and bcc for the other one, namely Cr–Ni (Fig. 1(c)) and Fe–Ni (Fig. 1(e)). Such regions are also present in ternary and quaternary alloys.

It should be noted that both fcc and bcc reference structures for Mn do not have $H_{form} = 0$, meaning that they are not ground states, see Fig. 1(b,d,f). The ground state for Mn is α -Mn, for which the unit cell consists of 58 atoms with four crystallographically inequivalent sites, each divided into two magnetically inequivalent sites, ordered antiferromagnetically. Since this is a complex phase, its stability is limited to the Mn-rich region [63], which is out of the scope of the

current work. Further in the paper, fcc Mn is considered as a reference for manganese.

Formation enthalpies for the whole bcc database, including ternary and quaternary structures, are presented in Supplementary Material, Fig. S1. Unlike for the fcc system, no stable ternary or quaternary intermetallic phases were found in the bcc Cr–Fe–Mn–Ni system from our DFT calculations. Stable intermetallic phases in fcc Cr–Fe–Mn–Ni alloys are given in Table II of Ref. [14].

4. Finite-temperature phase stability

In order to investigate the fcc-bcc phase stability of Cr–Fe–Mn–Ni alloys at elevated temperatures, the effective cluster interactions for the bcc system, described in the previous section, and for the fcc system, described in Ref. [14], were applied in MC simulations for a compositional grid, where the concentration of each element is changed in a step of 5 at.%, consisting of total 1767 compositions (excluding four compositions that are pure elements).

4.1. Fcc-bcc Gibbs free energy of formation difference

Gibbs free energies of formation were calculated based on formation enthalpies from MC simulations and configurational entropies obtained from pair correlation functions, as described in Section 2.1. Additionally, the magnetic and vibrational correction was applied to the fcc-bcc G_{form} difference from Ref. [42], also described in Section 2.1.

The calculations of configurational entropies using the pair-wise approximation for the first nearest neighbors (1NN) from Eqs. (11) and (12) produce reasonable entropy values in the high-temperature region (see Fig. 2(a)), approaching ideal values ($-k_B \sum_i c_i \ln c_i$), but often underestimate the entropy values in the low-temperature limit, where even negative values may be obtained [64]. Such negative values of entropy arise from the presence of long-range ordered precipitates forming in the alloy, for which, in practice, the entropy would be positive but low or close to zero. The thermodynamic integration method, on the other hand, does not produce the unphysical negative values of entropy S_{conf}^{TDI} at low temperatures approaching 0 K, however, in the high temperature limit, TDI produces values of entropy that deviate from ideal entropy, as discussed in Section 2.1. Moreover, TDI is significantly more time-consuming and, as such, is not used in this work for the whole composition space of Fe–Cr–Mn–Ni alloy.

Contributions to G_{form} are shown in Fig. S3(g,h) in Supplementary Material. The difference between G_{form}^{fcc} and G_{form}^{bcc} is shown in Fig. 2(b). As can be seen in this figure, the difference in G_{form} coming from 1NN pair-wise approximation is close to G_{form} calculated using TDI at temperatures above ~ 1100 K. When only positive values of 1NN entropy are considered, and negative values are equated to zero (below ~ 500 K), the difference of G_{form} between fcc and bcc phases is again similar for 1NN and TDI, unlike if no assumptions are made for negative entropies (green line in Fig. 2(b)).

Since negative entropy values are observed at different temperatures for fcc and bcc alloys of the same composition, the difference in the intermediate temperatures region is non-systematic and unreliable. Additionally, the Gibbs–Helmholtz relation, shown for equiatomic fcc and bcc alloys in Fig. S3 along with its description in Supplementary Material, also diverges in the intermediate temperatures region for Gibbs free energies with entropy calculated from pair-wise approximation. In the near-equiatomic region, which is of the main interest in this work, strong divergence, and fluctuations are observed for the Gibbs–Helmholtz relation at temperatures below 900 K. Considering these facts, the low-temperature results are unreliable with the error value, which is hard to estimate. Therefore, further in the paper, the analysis is performed for temperatures of 900 K and higher.

The effect of the correction G_{corr}^{Fe} , discussed at the end of Section 2.1 is also visible in Fig. 2: it increases the relative stability of fcc lattice (for

Fig. 1. Enthalpies of formation computed using DFT for (a) Cr–Fe (b) Cr–Mn, (c) Cr–Ni, (d) Fe–Mn, (e) Fe–Ni and (f) Mn–Ni binary structures underlying fcc and bcc lattice. Blue and red lines are the convex hull for the fcc and bcc systems, respectively. The black dashed lines join the most stable fcc and bcc structures and indicate the regions of possible coexistence of fcc and bcc phases at 0 K. (For interpretation of the references to color in this figure legend, the reader is referred to the web version of this article.)

(a)

(b)

Fig. 2. (a) Configurational entropies calculated using the pairwise approximation for the first nearest neighbors, S_{conf}^{1NN} , and the thermodynamic integration method, S_{conf}^{TDI} , for fcc and bcc equiatomic Cr–Fe–Mn–Ni alloy and (b) the difference of Gibbs free energy of formation between fcc and bcc phases for equiatomic Cr–Fe–Mn–Ni alloy (G_{diff}). Negative entropies in (a) are considered not physical, and as such, $S_{conf,positive}^{1NN}$ are considered in the calculations of G_{form} . In (b), $G_{diff,positive}^{1NN}$ is close to G_{diff}^{TDI} at low and high temperatures but not at intermediate temperatures. The effect of magnetic and vibrational correction for Fe, which helps to reproduce high-temperature γ -phase, is also visible in (b).

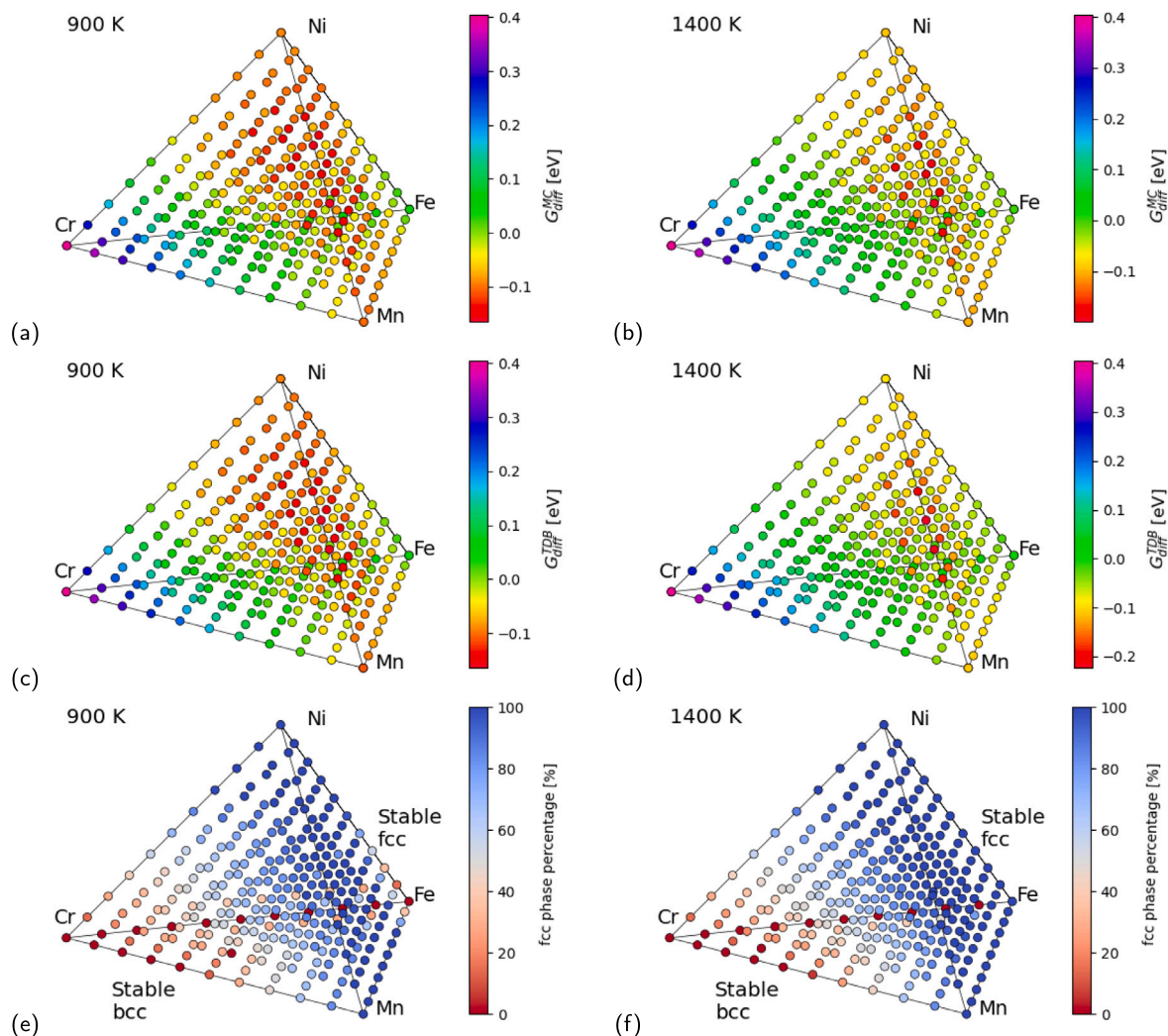


Fig. 3. The fcc-bcc G_{form} difference for the Cr-Fe-Mn-Ni alloys computed using (a,b) MC simulations and (c,d) TDB polynomials fitted on MC simulations at (a,c) 900 K and (b,d) 1400 K, respectively; (e,f) the fraction of fcc phase obtained by using the OpenCalphad calculations using TDB based on MC simulations at (e) 900 K and (f) 1400 K.

compositions with Fe) at higher temperatures and decreases its stability at lower temperatures.

In Fig. 3(a) and (b), there are shown the differences between the Gibbs free energies of formation for fcc and bcc alloys at temperatures 900 K and 1400 K, respectively, for the whole range of compositions. Values of differences between the Gibbs free energies of formation for fcc and bcc alloys for the whole composition range and investigated temperatures can be found in the accompanying dataset [65]. The fcc-bcc G_{form} differences have the most negative values for the Ni-rich alloys and the most positive values for the Cr-rich alloys. In the near-equiatomic region, the fcc-bcc G_{form} difference becomes smaller with the increase of temperature, but the fcc phase retains lower G_{form} values compared to the bcc phase. As it was shown in Ref. [26], the experimental results for $Cr_xFeMnNi$ alloys ($x = 0.8, 1.0, 1.2$ and 1.5) reveal that there is observed coexistence of two phases for a wide range of compositions.

4.2. Coexistence of fcc and bcc phases

In order to study the coexistence of fcc and bcc phases and their fractions in Cr-Fe-Mn-Ni alloys, we applied the method based on the development of TDBs and their application in the OpenCalphad calculations, described in Section 2.2.1.

The results of OpenCalphad calculations using TDB derived from MC simulations generally agree with those obtained directly from MC

simulations (see Fig. 3(c,d)). In Fig. 4, there is shown a comparison of Gibbs free energies of formation obtained using MC simulations and OpenCalphad calculations at 900 K and 1900 K for Fe-Ni binary system. While at high temperatures (Fig. 4(b)), where the alloy is disordered, the Gibbs free energy of formation curves for fcc and bcc alloys obtained using both methods are similar, at low temperatures (Fig. 4(a)), where there is present the $FeNi_3$ fcc intermetallic phase, there is a discrepancy between MC and TDB fitting on MC data.

The difference between the results obtained using the OpenCalphad calculations and MC simulations for the alloy compositions close to the known intermetallic phases, where the Gibbs free energies of formations decrease due to short-range ordering, is systematic and can be seen in other binary subsystems (see Supplementary Material, Fig. S4). As it is shown in Fig. 4(a) and Fig. S4 in Supplementary Material, the polynomials available in the `sqs2tdb` fitting cannot correctly reproduce the shape of the Gibbs free energy of formation curves close to the $CrNi_2$, $FeNi_3$, $MnNi_3$ and $MnNi$ phases, where the values from OpenCalphad diverge from the values obtained using the output of MC simulations. Since the same fitted polynomials describe the Gibbs free energy of the whole composition range, the divergence is also observed inside the four-component system, see Supplementary Material, Fig. S5.

As it was mentioned in Section 2.2, the equality of chemical potentials in binary alloys can be estimated using common tangent construction, and a subsequent lever rule application allows one to calculate the phase composition at any point in the temperature-composition space.

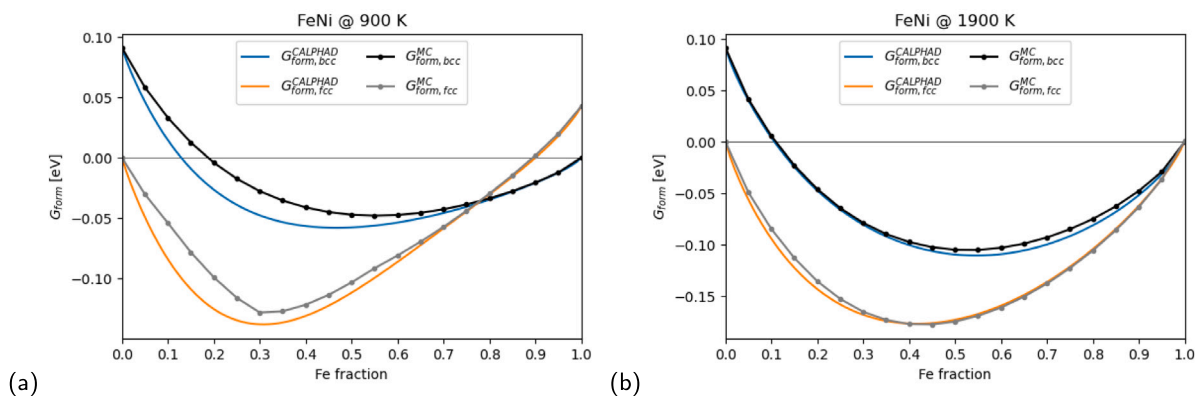


Fig. 4. The comparison of Gibbs free energies of formation calculated from MC simulations and the OpenCalphad calculations using TDB based on MC simulations at 900 K and 1900 K for bcc and fcc Fe-Ni binary alloys.

The difference in the estimation of the fcc phase fraction using raw MC output and calculated using fitted TDB for binary subsystems is shown in Fig. S6 in Supplementary Material. On average, OpenCalphad tends to underestimate the fraction of fcc phase in the alloy, and the root mean square error of the fcc fraction obtained from the fitted model is not higher than 4% above 1200 K (see Fig. S7 in the Supplementary Material), which will be taken as the error margin in the estimation of fcc fraction in the quaternary system.

As in the case of differences in G_{form} , there is a notable variation in the results at two temperatures: 900 K and 1400 K, compare Fig. 3(e) with Fig. 3(f). Apart from the fcc Ni-rich and bcc Cr-rich regions in composition space, there are visible points with the coexistence of fcc and bcc phase, which are located around the region where fcc-bcc G_{form} difference is almost equal to zero, shown in Fig. 3(c) and (d). Note that the atomic fraction of fcc and bcc phases was predicted by simulations for 1767 alloy compositions in the whole concentration range in the 5 at.% concentration mesh for the temperatures between 900 K and 1900 K. For the sake of clarity of presentation, the results are shown only for 10 at.% concentration mesh. Atomic fraction of fcc phase for all investigated temperatures and compositions is presented in the accompanying dataset [dataset] [65]. Note also that further in the text, an atomic fraction in theoretical results is simply referred to as a fraction.

4.3. The influence of element concentration on phase stability

In order to understand the influence of the concentration of each element on the fcc-bcc phase stability at the whole temperature range, we studied the temperature dependence of the fcc fraction in pseudobinary $[ABC]_{100-x}D_x$ alloys, where the concentration of one element, x , was varying from 0% to 100% with 5% concentration step and the concentrations of other elements were kept equiatomic.

The fcc fractions for pseudobinary alloys computed using the OpenCalphad calculations using TDB based on MC simulations (described in Section 2.2.1) are shown in Fig. 5(a)–(d). Similar to the Schaeffler diagram for Fe–Cr–Ni steels [66], in the case of Cr–Fe–Mn–Ni alloys, our results show an effect of stabilization of fcc and bcc phases by Ni and Cr, respectively, see 5(a,d).

According to our calculations, and taking into account error margin of 4% coming from MC to TDB fitting, the single fcc phase is fully stable in the considered range of temperatures for alloys with Cr content with 10 at.% Cr and lower, see Fig. 5(a). For alloys with Cr concentration higher than 90 at.% Cr above 900 K, single bcc phase is stable.

In contrary to Cr, Ni is a fcc phase stabilizer and the fcc phase is stable for the pseudobinary alloys with Ni content higher than 55 at.% at 1000 K and above, see Fig. 5(d). The fcc phase is dominant in the rest of Ni pseudobinary alloys.

As shown in Fig. 5(b), similarly to pure Fe, the fcc fraction of Fe-rich alloys is strongly dependent on temperature. The bcc fraction is dominant at lower temperatures, e.g., below 1100 K for the pseudobinary alloys with more than 90 at.% Fe, whereas at higher temperatures, the fcc phase becomes stable. The fcc-bcc phase transition temperature decreases with a decrease of Fe content. At the temperatures above 1700 K, the bcc iron becomes stable again. Between 1100 K and 1800 K for Fe concentrations of 50–90 at.%, single fcc phase region is observed.

The influence of Mn on the relative fcc-bcc phase stability of $[\text{CrFeNi}]_{100-x}\text{Mn}_x$ pseudobinary alloys is shown in Fig. 5(c). The investigation of that effect is potentially important for the design of Cr–Fe–Mn–Ni-based high-entropy alloys since those materials contain a significantly higher concentration of Mn than austenitic steels. Interestingly enough, the fcc phase is dominant for the whole Mn pseudobinary alloy. It should be noted that since α -Mn GS phase is not considered in this work, the phase of the structures in the Mn-rich region is not likely to be fcc, but rather α -Mn solid solution.

5. Experimental validation of the model

In order to validate the models, we compared the results of fcc-bcc phase stability of Cr–Fe–Mn–Ni alloys computed using DFT-based MC simulations with the experimental results available in the literature as well as those performed within this work.

5.1. Comparison with the experimental data from previous works

In Table 1, there are presented phase compositions of alloys investigated experimentally in Refs. [10,15,17,21–23,26,27,29] and compared with theoretical results obtained using the OpenCalphad method described in Section 2.2.1, which is based on DFT-based MC simulations. The results of MC simulations are given for temperatures corresponding to the annealing temperature of the considered experimental samples. As shown in Table 1, the fraction of the fcc phase obtained using the OpenCalphad method shows the same trend as the data from experimental observations. In particular, this theoretical model predicts no fraction of bcc phase for the alloy compositions characterized experimentally as single fcc phase from Refs. [15,22] and $\text{Cr}_4\text{Fe}_{40}\text{Mn}_{28}\text{Ni}_{28}$ alloy from Ref. [23], as well as predicts values within error margins of single fcc phase for alloys with 35 at.% Fe from Ref. [21] and $\text{Cr}_{12}\text{Fe}_{40}\text{Mn}_{28}\text{Ni}_{20}$ alloy from Ref. [23]. For the rest of the structures, the fcc percentage values predicted by the OpenCalphad model are underestimated compared to the experimental data, as discussed in Section 4.2. However, the trends generally agree with the experimental sets of data from various works, e.g., our model (1) predicts the decrease of stability of the fcc phase with the increase of Cr content in the alloy reported in Ref. [26]; predicts on average higher fcc fractions for alloy compositions that were reported as single fcc phase

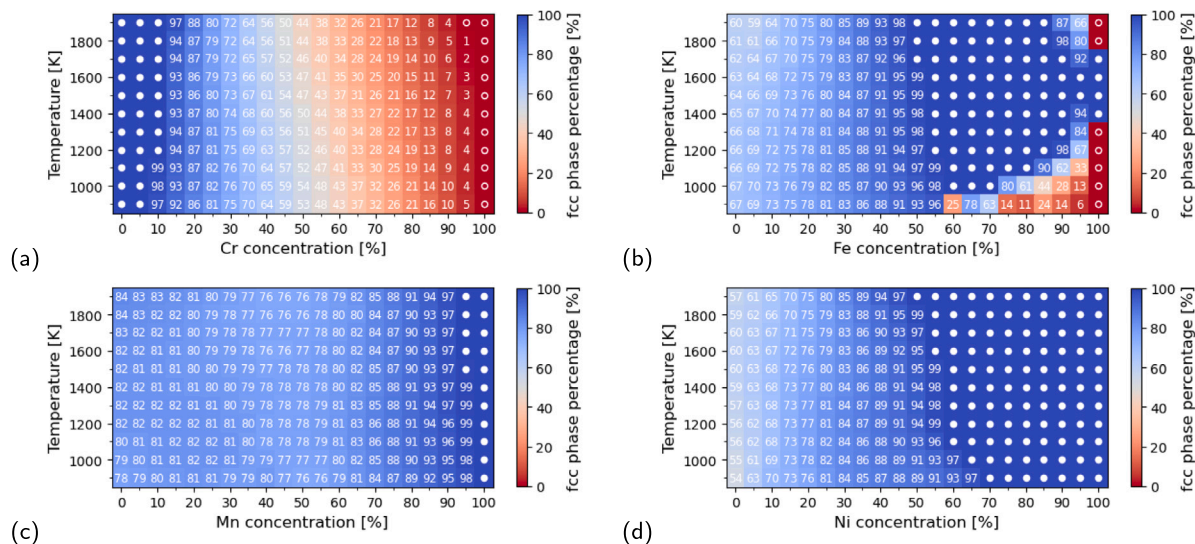


Fig. 5. Temperature-composition heatmaps showing fcc fraction in the Cr–Fe–Mn–Ni alloys according to the OpenCalphad calculations using TDB based on MC simulations as a function of temperature and composition of [ABC]_{100-x}D_x pseudobinary alloys for D being (a) Cr, (b) Fe, (c) Mn and (d) Ni. In order to improve the readability of the figure, 100% fcc is marked with filled circles (•), and 0% fcc is marked with open circles (○).

Table 1

Comparison of percentage of fcc phase [in %] for the alloys in the Cr–Fe–Mn–Ni system given in the literature with the values obtained using OpenCalphad calculations with TDB based on the results of MC simulations (MC+TDB), described in Section 2.2.1. For the samples that were heat-treated at different temperatures, phase composition are presented for the temperature of MC simulations performed with 100 K step close to the temperature of the final heat treatment, shown in the last column [in K]. “<100” means that the experiment shows the coexistence of fcc phase with another phase, but the fcc fraction was not provided in the reference.

Composition	Treatment	Expt.	MC+TDB	T
Cr ₁₂ Fe ₆₄ Mn ₁₂ Ni ₁₂	[15] homogenized at 1473 K 10 h, air-cooled, cold-rolled (50%), annealed at 1273 K for 1 h	100	100	1300
Cr ₁₂ Fe ₆₀ Mn ₁₆ Ni ₁₂		100	100	1300
Cr ₁₂ Fe ₅₆ Mn ₂₀ Ni ₁₂		100	100	1300
Cr ₁₈ Fe ₂₉ Mn ₂₃ Ni ₃₀	[17] homogenized at 1473 K 18 h, quenched	100	91	1500
Cr ₂₀ Fe ₃₅ Mn ₀ Ni ₄₅	[21] annealed at 1373 K 24 h, cold-rolled (80%), annealed at 1173 K 1 h, gas-quenched	100	97	1200
Cr ₂₀ Fe ₃₀ Mn ₅ Ni ₄₅		100	95	1200
Cr ₂₀ Fe ₃₅ Mn ₅ Ni ₄₀		100	96	1200
Cr ₂₀ Fe ₃₀ Mn ₁₀ Ni ₄₀		100	94	1200
Cr ₁₃ Fe ₅₀ Mn ₂₇ Ni ₁₀	[22] cold-rolled, annealed at 1173 K 1 h	100	95	1200
Cr ₄ Fe ₄₀ Mn ₂₈ Ni ₂₈	[23] homogenized at 1273 K 24 h, cold-rolled (80%), annealed at 1123 K 30m	100	100	1100
Cr ₁₂ Fe ₄₀ Mn ₂₈ Ni ₂₀		100	97	1100
Cr ₁₈ Fe ₄₀ Mn ₂₈ Ni ₁₄		100	87	1100
Cr ₂₄ Fe ₄₀ Mn ₂₈ Ni ₈		<100	76	1100
Cr ₂₁ Fe ₂₆ Mn ₂₆ Ni ₂₆	[26] homogenized at 1473 K 6 h, forged, annealed at 1073 K 1 h	100	86	1100
Cr ₂₅ Fe ₂₅ Mn ₂₅ Ni ₂₅		99	82	1100
Cr ₂₉ Fe ₂₄ Mn ₂₄ Ni ₂₄		91	77	1100
Cr ₃₃ Fe ₂₂ Mn ₂₂ Ni ₂₂		77	72	1100
Cr ₂₀ Fe ₃₅ Mn ₁₀ Ni ₃₅	[27] water-cooled, homogenized at 1273 K 12 h, water-cooled	100	95	1300
Cr ₁₈ Fe ₂₇ Mn ₂₇ Ni ₂₈	[10] homogenized at 1473 K for 48 h, cold rolled, recrystallized at 1173 K for 4 h	100	90	1200
Cr ₃₇ Fe ₃₃ Mn ₁₂ Ni ₁₉	[29] homogenized in a water-cooled vacuum furnace (base pressure ~10 ⁻⁶ torr) at 1273 K for 24 h followed by furnace cooling to room temperature at an average cooling rate of approximately 1 K/s	<100	71	1300
Cr ₄₂ Fe ₁₇ Mn ₂₀ Ni ₂₂		<100	61	1300
Cr ₃₆ Fe ₁₃ Mn ₁₂ Ni ₄₀		<100	74	1300
Cr ₂₁ Fe ₃₅ Mn ₂₄ Ni ₂₀		100	88	1300
Cr ₁₉ Fe ₃₁ Mn ₁₁ Ni ₃₈		100	95	1300
Cr ₂₅ Fe ₁₄ Mn ₂₄ Ni ₃₈		100	81	1300
Cr ₂₃ Fe ₂₆ Mn ₁₉ Ni ₃₂		100	86	1300
Cr ₃₃ Fe ₁₅ Mn ₂₀ Ni ₃₂		<100	73	1300
Cr ₂₅ Fe ₂₉ Mn ₁₆ Ni ₃₀		<100	85	1300
Cr ₃₁ Fe ₂₇ Mn ₂₂ Ni ₂₁		<100	74	1300

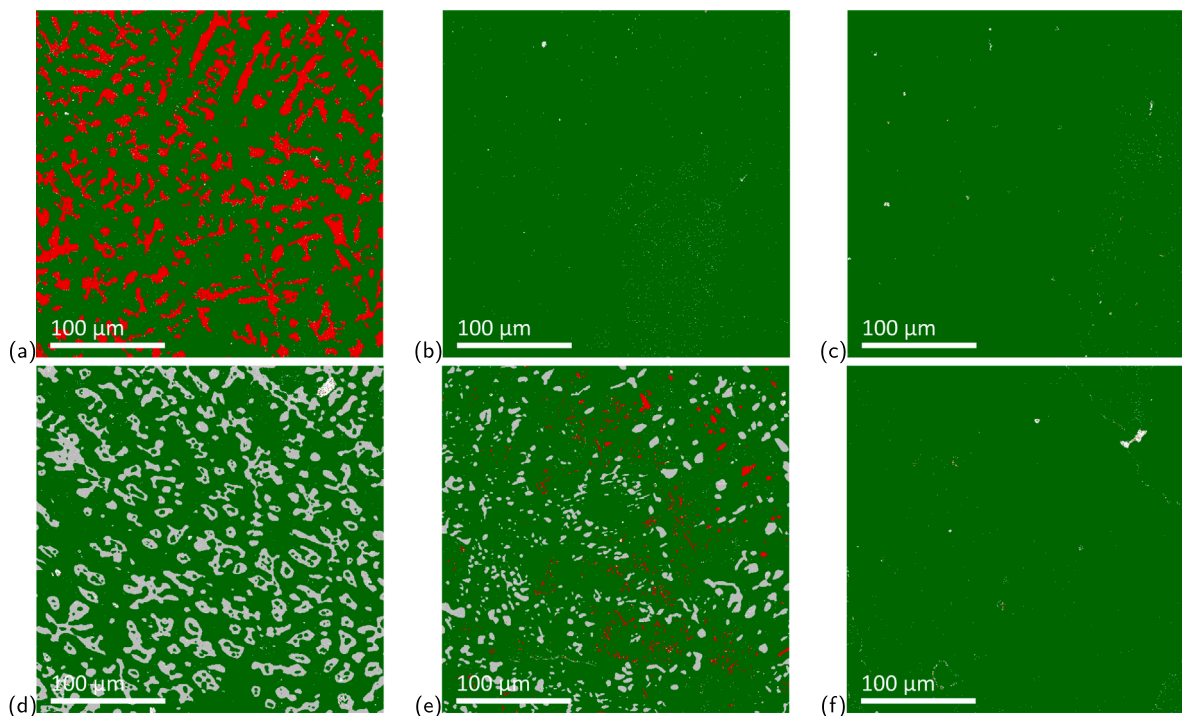


Fig. 6. The results of EBSD characterization of the (a–c) as-cast and (d–f) annealed samples of alloys with (a,d) 20, (b,e) 25 and (c,f) 35 at.% Ni. Green, red and gray colors indicate the fcc, bcc and σ phases, respectively. (For interpretation of the references to color in this figure legend, the reader is referred to the web version of this article.)

in experimental investigation from Ref. [29] and lower fractions for the multiphase alloy compositions from the same work. It should be noted that another potential source of the difference in the predicted and experimental results can be the relatively short annealing time in experiments that might not be enough to reach the thermodynamic equilibrium state simulated using the exchange MC simulations, to which the thermodynamic database was fitted.

5.2. Comparison with the experiments performed within this work

Since Ni is the main fcc stabilizer and, as was shown in Ref. [14], it has the most prominent impact on the order–disorder transition temperature, we performed additional experiments in this work on $[\text{CrFeMn}]_{100-x}\text{Ni}_x$ pseudobinary alloys in order to improve the understanding of the effect of Ni on the phase stability of the Cr–Fe–Mn–Ni alloys and to validate our model. We focused attention on three Ni concentrations: 20, 25 and 35 at. % Ni, with other elements kept equiatomic. Samples of respective alloys were synthesized using arc-melting and annealed at 1273 K for 48 h, as described in Section 2.4.

Results of EBSD characterization of as-cast and annealed samples are shown in Fig. 6. It can be noted that in the case of as-cast samples, a two-phase structure with fcc and bcc phases is observed only for $[\text{CrFeMn}]_{80}\text{Ni}_{20}$ alloy, see Fig. 6(a). For higher concentrations of Ni (25 and 35 at. %), a single fcc phase is observed – Fig. 6(b) and (c). Thus, contrary to results reported in Refs. [18,19,24,26], no decomposition of the as-cast equiatomic fcc Cr–Fe–Mn–Ni alloy into bcc or σ phases. On the other hand, such a decomposition is visible in the EBSD patterns for the annealed sample of equiatomic alloy. It is worth noting that there is a coexistence of three phases, namely fcc, bcc and σ phase. The presence of the σ phase within the fcc high entropy alloys with Cr–Fe, Cr–Mn subsystems and ternary Cr–Fe–Mn one [67,68] was reported recently in Refs. [3,69–71]. In the Cantor alloy, the σ phase is found to

be significantly enriched with Cr, and also contained some Mn, Fe and Co, while the concentration of Ni was very low. The crystal structure of this phase was found to be tetragonal, with lattice parameters of $a \approx 8.8 \text{ \AA}$ and $c \approx 4.5 \text{ \AA}$ [69], consistent with the well-known σ phase in Cr–Fe binary ($a = 8.799 \text{ \AA}$ and $c = 4.546 \text{ \AA}$) [72]. The latter is related to the A2 (bcc solid solution) kinetic phase transformation from the high-temperature phase [73]. Analyzing the results of EBSD, SEM and EDS investigations, it can be concluded that in the case of alloy with 20 at. % Ni, the bcc phase observed in the as-cast sample is transformed into the σ phase by annealing applied to as-cast samples, compare Fig. 6(a) and (d). The $[\text{CrFeMn}]_{65}\text{Ni}_{35}$ alloy is a single fcc phase both for the as-cast sample as well as the annealed sample.

The area fractions of fcc, bcc and σ phase in the as-cast and annealed samples of Cr–Fe–Mn–Ni alloy are summarized in Table 2 and compared with theoretical results obtained using the method described in Section 2.2.1. Since we were not able to determine reference temperature for as-cast samples, unlike in the post-casting annealing, the experimental data are compared with the results computed using both methods for temperatures between 1000 K and 1400 K.

In agreement with the results from EBSD characterization, the lowest fraction of the fcc phase obtained from our theoretical method is observed for the alloy with 20 at. % Ni. The theoretical values derived using OpenCalphad based on the results of MC simulations agree with experimental results for the as-cast sample and are slightly overestimated for the annealed sample. For the equiatomic alloy, an increase of fcc fraction compared to the $[\text{CrFeMn}]_{80}\text{Ni}_{20}$ alloy is observed, however, the phase composition is not the single fcc phase for most temperatures analyzed, see Fig. 5(d). It may suggest that the as-cast sample of alloy characterized as a single fcc phase is probably not in a thermodynamic equilibrium state. This is confirmed by the EBSD result for the sample of equiatomic alloy annealed at 1273 K for 48 h, for which the fcc fraction is 87.5% which is close to the OpenCalphad estimates, latter providing fcc fraction equal to 81%, which is expected to be an underestimation. The fraction of fcc phase for the alloy with

Table 2

The area fractions of phases [in %] measured using EBSD and their average compositions measured using EDS for the as-cast and annealed samples of considered alloys compared with the atomic fractions of fcc and bcc phases obtained using the OpenCalphad calculations with TDB based on the results of MC simulations (MC+TDB), described in Section 2.2.1. Since the temperature related to the as-cast state is unknown, the experimental data are compared with the MC+TDB results for the range of temperatures between 1000 K and 1400 K, inclusively, and the data is presented not for the endpoints but for minimum and maximum values observed in this range.

Target composition	Experiment		MC+TDB
	Composition	Phase %	Phase %
As-cast (MC @ 1000–1400 K)			
[CrFeMn] ₈₀ Ni ₂₀	Cr _{20.8} Fe _{23.8} Mn _{31.3} Ni _{24.7}	77.5 fcc	77–78 fcc
	Cr _{33.6} Fe _{28.6} Mn _{23.5} Ni _{14.3}	21.8 bcc	22–23 bcc
[CrFeMn] ₇₅ Ni ₂₅	Cr _{23.1} Fe _{26.7} Mn _{24.2} Ni _{24.1}	100 fcc	80–82 fcc
			18–20 bcc
[CrFeMn] ₆₅ Ni ₃₅	Cr _{21.2} Fe _{20.4} Mn _{22.6} Ni _{35.8}	100 fcc	86–87 fcc
			13–14 bcc
Annealed (Expt. @ 1273 K, MC @ 1300 K)			
[CrFeMn] ₈₀ Ni ₂₀	Cr _{20.1} Fe _{27.1} Mn _{28.6} Ni _{24.1}	75 fcc	77 fcc
	Cr _{40.9} Fe _{27.2} Mn _{21.5} Ni _{10.5}	23.8 σ	23 bcc
[CrFeMn] ₇₅ Ni ₂₅	Cr _{21.3} Fe _{25.9} Mn _{26.1} Ni _{26.7}	87.5 fcc	81 fcc
	Cr _{43.4} Fe _{26.0} Mn _{18.9} Ni _{11.8}	10.4 σ	19 bcc
[CrFeMn] ₆₅ Ni ₃₅	Cr _{79.9} Fe _{2.0} Mn _{9.6} Ni _{3.6}	1.53 bcc	
	Cr _{21.3} Fe _{21.9} Mn _{22.0} Ni _{34.8}	99.6 fcc	87 fcc
			13 bcc

35 at.% Ni is 100% for the as-cast and 99.6% for the annealed sample, while the results computed using the OpenCalphad method based on the results of MC simulations gives underestimated values of 86–87%.

The results of SEM combined with EDS investigations show that multi-phase alloys of fcc, bcc and phases are decomposed usually into the Ni-rich fcc regions and the Cr-rich regions of the bcc or σ phase. As shown in Fig. 7(a)–(f), the Cr-rich regions are usually depleted of Ni and *vice versa*. Mn and Fe are distributed much more uniformly in the investigated alloys, however, their concentrations are, in general, more correlated with the presence of Ni, see Fig. 7(g)–(l).

As shown in Table 2, the composition of the σ phase, measured using EDS, is similar for both samples where it exists, namely for the annealed samples with Ni concentrations equal to 20% and 25%. The average concentrations of Cr and Fe are slightly higher than 40 at. % and 25 at. %, respectively, and the concentrations of Mn and Ni are approximately 20 at. % and 10 at. %, respectively. The average compositions of the fcc and bcc phases vary depending on the nominal composition of the alloy and depending on whether the sample was annealed or not. However, for all the considered alloy compositions, the average concentration of Cr in the fcc phase is smaller than 23.1 at. % and 21.3 at. % for the as-cast and annealed samples, respectively. For the case of the bcc phase, the difference between the phase composition for the as-cast [FeCrMn]₈₀Ni₂₀ and the annealed [FeCrMn]₇₅Ni₂₅ sample is notable. The average concentration of Cr in the latter one is approximately 80 at. % and it is more than two times larger than the value measured for the former one. As a consequence, the concentration of other elements in the annealed [FeCrMn]₇₅Ni₂₅ sample is small with only 3.6 at. % Ni, whereas their concentrations in the as-cast [FeCrMn]₈₀Ni₂₀ sample is closer to the nominal concentration with a decrease concentration of Ni equal to 14.3 at. %.

6. Prediction of new single fcc phases

As was shown in the previous sections, the OpenCalphad calculations using TDBs fitted on results of DFT-based MC simulations enable an understanding of the influence of concentrations of constituent elements on the fcc-bcc phase stability of Cr–Fe–Mn–Ni alloys. Moreover, the OpenCalphad calculations can be applied to design new near-equiatomic compositions of high-entropy alloys for which the stability of a single fcc phase will be maintained for a relatively wide range of

temperatures. Since the method based on the development of thermodynamic databases and the application of the OpenCalphad calculations underestimate the stability of the fcc phase not in a systematic manner, a safe error margin for selecting alloys with a single fcc phase is an error margin from binary system predictions equal to 4% (described in Section 4.2).

In Fig. 8, fcc fractions are shown as a temperature function for the alloy compositions, for which the fcc phase is fully stable (within error margin) at temperatures above 1000 K and are located in the near-equiatomic region, more specifically, for which the concentrations of each element, x , lie within the range $35 \geq x \geq 10$ at. %, and min and max range limits each may be reached only by one element. The alloy with the composition of ORNL sample, Cr₁₈Fe₂₈Mn₂₆Ni₂₈, is also presented in the figure for reference, as this alloy has been reported to have single fcc phase in Ref. [10] and later shown to possess high irradiation resistance. In line with the knowledge that Ni and Cr are the fcc and bcc stabilizers, respectively, in the near-equiatomic region there is only one composition with 25 at.% Ni – others having higher nickel concentration –, and the concentrations of Cr is not higher than 15 at.%. Fe and Mn concentrations lie in the range 25–35 at.%. Among the presented alloys, Cr₁₀Fe₃₅Mn₂₅Ni₃₀ possesses single fcc phase in the 1000–1900 K temperature region. This alloy, as compared to the ORNL alloy, has decreased concentration of Cr and Mn – 8 and 2 at.%, respectively, which are traded for the increased concentrations of 8 and 2 at.% of Fe and Ni, respectively.

7. Conclusions

- The cluster expansion model developed for bcc Cr–Fe–Mn–Ni alloys parametrized based on parameters determined from density functional theory (DFT) calculations and the application of the fcc model for these alloys from Ref. [14] enabled to investigate relative phase stability of fcc and bcc phases in Cr–Fe–Mn–Ni alloys using Monte Carlo (MC) simulations and OpenCalphad calculations using the thermodynamic databases (TDBs), fitted to the excess Gibbs free energies obtained in the MC simulations.
- The differences between the Gibbs free energies of the formation of fcc and bcc alloys are the most negative for Ni-rich alloys and the most positive for Cr-rich alloys.
- The coexistence of the fcc and bcc phases as well as estimates of fractions of both phases in Cr–Fe–Mn–Ni alloys were studied using the method based on the development of TDBs derived from MC simulations and their application in the OpenCalphad calculations.
- The values of fcc phase percentage obtained using OpenCalphad calculations based on TDBs from MC simulations are usually underestimated in comparison with the experimental results reported in the literature and performed in this work.
- The coexistence of the fcc and bcc phases is predicted for a relatively wide range of compositions and temperatures. The coexistence of two phases is observed in the pseudobinary [FeMnNi]_{100-x}Cr_x alloys for concentrations between 10 and 95 at.% Cr whereas in the [CrFeMn]_{100-x}Ni_x alloys for Ni concentration smaller than 60 at.%.
- The present study shows that the fcc phase is found to be dominant for the pseudobinary alloy [CrFeNi]_{1-x}Mn_x with all considered Mn concentrations and temperatures.
- The fcc fractions computed using OpenCalphad calculations for the alloy with 20 at.% Ni are generally in line with the values measured using EBSD for the as-cast and annealed sample.
- The OpenCalphad calculations for the equiatomic alloy revealed no single fcc phase region for all of the temperatures considered. It agrees with the EBSD characterization for the annealed sample, but disagrees with the results for the as-cast samples. It may suggest that the as-cast sample is not in a thermodynamic equilibrium state.

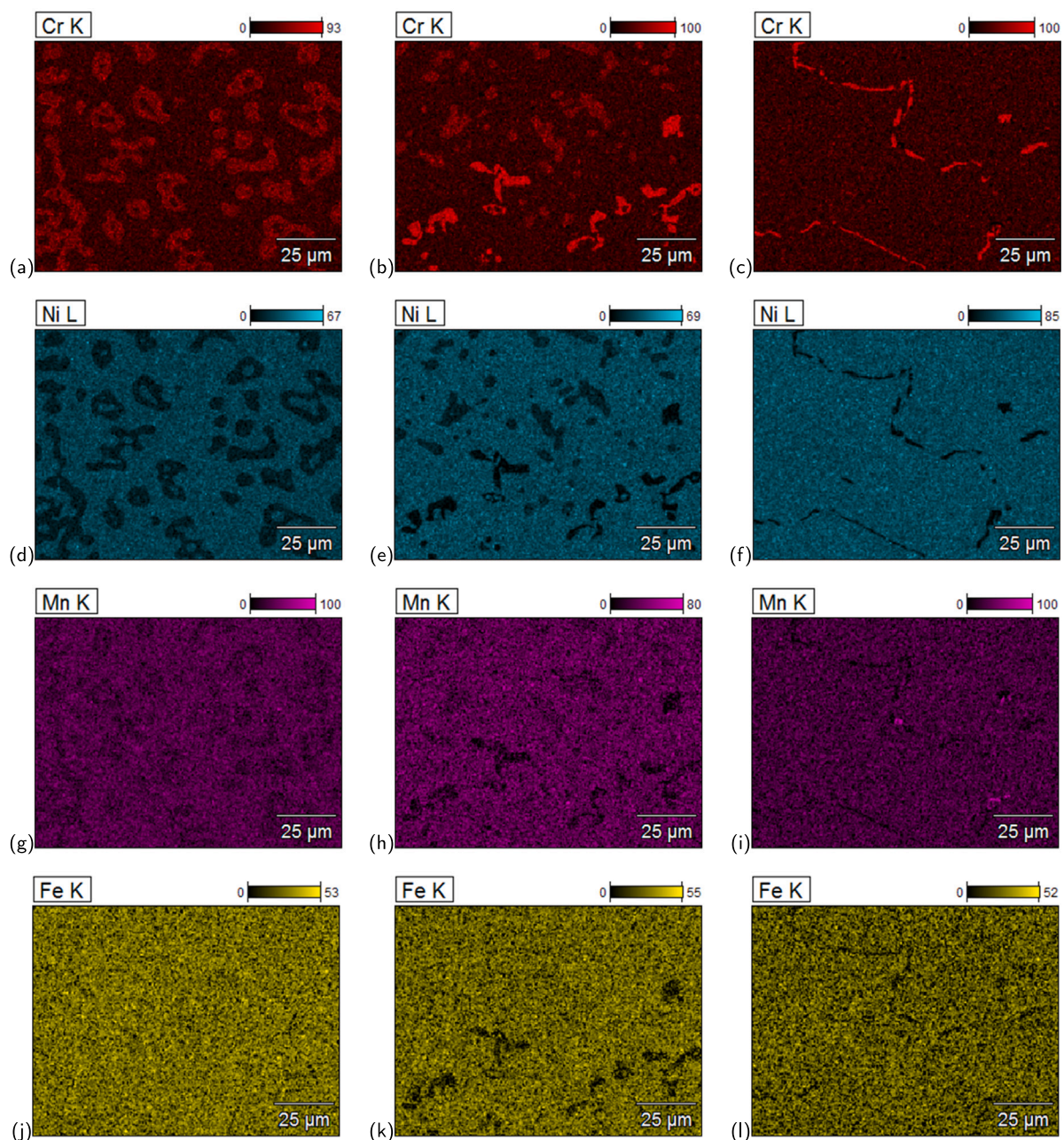


Fig. 7. EDS mapping of (a–c) Cr, (d–f) Ni, (g–i) Mn and (j–l) Fe for the annealed samples of alloys with (a,d,g,j) 20, (b,e,h,k) 25 and (c,f,i,l) 35 at.% Ni.

- During post-casting annealing, the bcc phase observed in the as-cast samples of alloys is transformed (or partially transformed) into the sigma phase while the fraction of the fcc phase is not significantly changed.
- The DFT-based MC simulations combined with the TDB fitting and OpenCalphad calculations enabled to propose the near-equiatomic alloy compositions that are single fcc phase for a wide range of temperatures, which might be potentially interesting for further research. Among them, $\text{Cr}_{10}\text{Fe}_{35}\text{Mn}_{25}\text{Ni}_{30}$ possesses the fcc phase percentage equal to 100% in the whole considered range of temperatures.

Declaration of competing interest

The authors declare that they have no known competing financial interests or personal relationships that could have appeared to influence the work reported in this paper.

Acknowledgments

Studies were funded by Materials Technologies project granted by Warsaw University of Technology, Poland under the program Excellence Initiative: Research University (ID-UB). The simulations were carried out with the support of the Interdisciplinary Centre for Mathematical and Computational Modelling (ICM), University of Warsaw, under grant No. GB79-6. DNM work has been carried out within the framework of the EUROfusion Consortium, funded by the European Union via the Euratom Research and Training Programme (Grant Agreement No 101052200 — EUROfusion). Views and opinions expressed are however those of the author(s) only and do not necessarily reflect those of the European Union or the European Commission. Neither the European Union nor the European Commission can be held responsible for them. DNM also acknowledges funding from the RCUK Energy Programme Grant No. EP/W006839/1. We acknowledge the

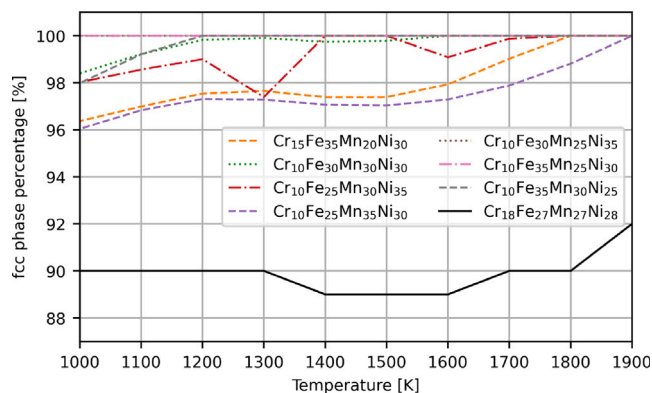


Fig. 8. Percentage of fcc in the near-equiatomic Cr-Fe-Mn-Ni alloys. All presented compositions have the percentage of fcc phase that is equal to or below 100% not more than the expected error of 4%, estimated in Section 4.2. The ORNL composition from Ref. [10], $\text{Cr}_{18}\text{Fe}_{27}\text{Mn}_{27}\text{Ni}_{28}$ (black solid line) is presented for reference.

support from the European Union Horizon 2020 research and innovation program under NOMATEN Teaming grant agreement no. 857470 and from the European Regional Development Fund via the Foundation for Polish Science International Research Agenda Plus program grant no. MAB PLUS/2018/8, which partially covered the salary of Witold Chrominski. DNM and JSW also would like to thank the support from high-performing computing facility MARCONI (Bologna, Italy) provided by EUROfusion. We would also like to thank Damian Sobieraj for his help with the preparation of samples and Prof. Bo Sundman for helpful discussion on OpenCalphad forum. DNM wishes to thank Adrien Couet for exchange communication on his high-throughput works in Cr-Fe-Mn-Ni alloys.

Appendix A. Supplementary data

Supplementary material related to this article can be found online at <https://doi.org/10.1016/j.actamat.2023.119047>.

References

- [1] B. Cantor, I.T.H. Chang, P. Knight, A.J.B. Vincent, Microstructural development in equiatomic multicomponent alloys, *Mater. Sci. Eng. A* 375–377 (2004) 213–218.
- [2] J.-W. Yeh, S.-K. Chen, S.-J. Lin, J.-Y. Gan, T.-S. Chin, T.-T. Shun, C.-H. Tsau, Nanostructured high-entropy alloys with multiple principal elements: Novel alloy design concepts and outcomes, *Adv. Eng. Mater.* 6 (5) (2004) 299–303.
- [3] E.K. Pickering, N.G. Jones, High-entropy alloys: A critical assessment of their founding principles and future prospects, *Int. Mater. Rev.* 61 (3) (2016) 183–202.
- [4] D.B. Miracle, O.N. Senkov, A critical review of high entropy alloys and related concepts, *Acta Mater.* 122 (2017) 448–511.
- [5] E.P. George, W.A. Curtin, C.C. Tasan, High entropy alloys: A focused review of mechanical properties and deformation mechanisms, *Acta Mater.* 188 (2020) 435–474.
- [6] Y. Shi, B. Yang, P.K. Liaw, Corrosion-resistant high-entropy alloys: A review, *Metals* 7 (2) (2017) 1–18.
- [7] A.V. Kuznetsov, D.G. Shaysultanov, N.D. Stepanov, G.A. Salishchev, O.N. Senkov, Tensile properties of an AlCrCuNiFeCo high-entropy alloy in as-cast and wrought conditions, *Mater. Sci. Eng. A* 533 (2012) 107–118.
- [8] O.N. Senkov, S.V. Senkova, C. Woodward, Effect of aluminum on the microstructure and properties of two refractory high-entropy alloys, *Acta Mater.* 68 (2014) 214–228.
- [9] F.J. Wang, Y. Zhang, G.L. Chen, Atomic packing efficiency and phase transition in a high entropy alloy, *J. Alloys Compd.* 478 (1–2) (2009) 321–324.
- [10] N.A.P. Kiran Kumar, C. Li, K.J. Leonard, H. Bei, S.J. Zinkle, Microstructural stability and mechanical behavior of FeNiMnCr high entropy alloy under ion irradiation, *Acta Mater.* 113 (2016) 230–244.
- [11] C. Lu, L. Niu, N. Chen, K. Jin, T. Yang, P. Xiu, Y. Zhang, F. Gao, H. Bei, S. Shi, M.-R. He, L.M. Robertson, W.J. Weber, L. Wang, Enhancing radiation tolerance by controlling defect mobility and migration pathways in multicomponent single-phase alloys, *Nature Commun.* 7 (2016) 13564.

- [12] K. Jin, C. Lu, L.M. Wang, J. Qu, W.J. Weber, Y. Zhang, H. Bei, Effects of compositional complexity on the ion-irradiation induced swelling and hardening in Ni-containing equiatomic alloys, *Scr. Mater.* 119 (2016) 65–70.
- [13] O. El-Atwani, N. Li, M. Li, A. Devaraj, J.K.S. Baldwin, M.M. Schneider, D. Sobieraj, J.S. Wróbel, D. Nguyen-Manh, S.A. Maloy, E. Martinez, Outstanding radiation resistance of tungsten-based high-entropy alloys, *Sci. Adv.* 5 (3) (2019) eaav2002.
- [14] M. Fedorov, J.S. Wróbel, A. Fernández-Caballero, K.J. Kurzydowski, D. Nguyen-Manh, Phase stability and magnetic properties in fcc Fe-Cr-Mn-Ni alloys from first-principles modeling, *Phys. Rev. B* 101 (2020) 174416.
- [15] D.H. Chung, W.C. Kim, S.Y. Baek, M.H. Kim, Y.S. Na, Thermodynamics-based design strategy for optimizing strength and ductility of Cr-Ni-Mn-Fe medium-entropy alloys, *J. Alloys Compd.* 899 (2022) 163331.
- [16] A. Fernández-Caballero, E. Bousser, S.M. Shubeita, P.T. Wady, Y. Gu, R. Krishna, M.J. Gorley, D. Nguyen-Manh, P.M. Mummery, E.J. Pickering, High-dose ion irradiation damage in $\text{Fe}_{38}\text{Ni}_{38}\text{Mn}_{26}\text{Cr}_{18}$ characterized by TEM and depth-sensing nanoindentation, *Nucl. Mater. Energy* 28 (2021) 101028.
- [17] A. Kamboj, E.A. Marquis, Effect of dose rate on the phase stability of a CrFeNiMn alloy, *Scr. Mater.* 215 (2022) 114697.
- [18] J. Lehtonen, Y. Ge, N. Ciftci, O. Heczko, V. Uhlenwinkel, S.-P. Hannula, Phase structures of gas atomized equiatomic CrFeNiMn high entropy alloy powder, *J. Alloys Compd.* 827 (2020) 154142.
- [19] J. Lehtonen, P. Lehto, Y. Ge, A. Juselius, S.-P. Hannula, Mechanical properties of pulsed electric current sintered CrFeNiMn equiatomic alloy, *Mater. Sci. Eng. A* 842 (2022) 143071.
- [20] C. Li, X. Hu, T. Yang, N.A.P. Kiran Kumar, B.D. Wirth, S.J. Zinkle, Neutron irradiation response of a co-free high entropy alloy, *J. Nucl. Mater.* 527 (2019) 151838.
- [21] T.J. Manescau, J. Braun, O. Dezellus, Computational development, synthesis and mechanical properties of face centered cubic Co-free high entropy alloys, *Mater. Today Commun.* 30 (2022) 103202.
- [22] R.K. Nutor, M. Azeemullah, Q.P. Cao, X.D. Wang, D.X. Zhang, J.Z. Jiang, Microstructure and properties of a Co-free $\text{Fe}_{50}\text{Mn}_{27}\text{Ni}_{10}\text{Cr}_{13}$ high entropy alloy, *J. Alloys Compd.* 851 (2021) 156842.
- [23] N.D. Stepanov, D.G. Shaysultanov, M.A. Tikhonovsky, G.A. Salishchev, Tensile properties of the Cr-Fe-Ni-Mn non-equiatomic multicomponent alloys with different Cr contents, *Mater. Des.* 87 (2015) 60–65.
- [24] Z. Wu, H. Bei, F. Otto, G.M. Pharr, E.P. George, Recovery, recrystallization, grain growth and phase stability of a family of FCC-structured multi-component equiatomic solid solution alloys, *Intermetallics* 46 (2014) 131–140.
- [25] Z. Wu, H. Bei, Microstructures and mechanical properties of compositionally complex Co-free FeNiMnCr₁₈ FCC solid solution alloy, *Mater. Sci. Eng. A* 640 (2015) 217–224.
- [26] Y. Zhang, H. Wu, X. Yu, D. Tang, R. Yuan, H. Sun, Microstructural evolution and strengthening mechanisms in Cr_xMnFeNi high-entropy alloy, *J. Mater. Res. Technol.* 12 (2021) 2114–2127.
- [27] J. Zhou, H. Liao, H. Chen, A. Huang, Microstructure and tensile mechanical behavior of a single-phase $\text{Fe}_{35}\text{Mn}_{10}\text{Cr}_{20}\text{Ni}_{35}$ high-entropy alloy, *J. Mater. Eng. Perform.* 30 (5) (2021) 3352–3362.
- [28] A. Daramola, G. Bonny, G. Adjanor, C. Domain, G. Monnet, A. Fraczkiewicz, Development of a plasticity-oriented interatomic potential for CrFeMnNi high entropy alloys, *Comput. Mater. Sci.* 203 (2022) 111165.
- [29] M. Moorehead, P. Nelaturu, M. Elbakshshwan, C. Parkin, C. Zhang, K. Sridharan, D.J. Thoma, A. Couet, High-throughput ion irradiation of additively manufactured compositionally complex alloys, *J. Nucl. Mater.* 547 (2021) 152782.
- [30] A. Couet, Integrated high-throughput research in extreme environments targeted toward nuclear structural materials discovery, *J. Nucl. Mater.* 559 (2022) 153425.
- [31] B. Sundman, U.R. Kattner, M. Palumbo, S.G. Fries, OpenCalphad - a free thermodynamic software, *Integr. Mater. Manuf. Innov.* 4 (1) (2015) 1–15.
- [32] J.S. Wróbel, D. Nguyen-Manh, M.Y. Lavrentiev, M. Muzyk, S.L. Dudarev, Phase stability of ternary fcc and bcc Fe-Cr-Ni alloys, *Phys. Rev. B* 91 (2015) 024108.
- [33] D. Sobieraj, J.S. Wróbel, T. Rygiel, K.J. Kurzydowski, O. El-Atwani, A. Devaraj, E. Martinez Saez, D. Nguyen-Manh, Chemical short-range order in derivative Cr-Ta-Ti-V-W high entropy alloys from the first-principles thermodynamic study, *Phys. Chem. Chem. Phys.* 22 (2020) 23929–23951.
- [34] D. Nguyen-Manh, J.S. Wróbel, M. Klimenkov, M.J. Lloyd, L. Messina, S.L. Dudarev, First-principles model for voids decorated by transmutation solutes: Short-range order effects and application to neutron irradiated tungsten, *Phys. Rev. Mater.* 5 (2021) 065401.
- [35] A. van de Walle, Multicomponent multisublattice alloys, nonconfigurational entropy and other additions to the alloy theoretic automated toolkit, *CALPHAD* 33 (2) (2009) 266–278.
- [36] A. Fernández-Caballero, M. Fedorov, J.S. Wróbel, P.M. Mummery, D. Nguyen-Manh, Configurational entropy in multicomponent alloys: Matrix formulation from Ab initio based Hamiltonian and application to the FCC Cr-Fe-Mn-Ni system, *Entropy* 21 (1) (2019) 68.
- [37] A. van de Walle, G. Ceder, The effect of lattice vibrations on substitutional alloy thermodynamics, *Rev. Modern Phys.* 74 (January) (2002) 11–45.

- [38] M.E.J. Newman, G.T. Barkema (Eds.), Monte Carlo Methods in Statistical Physics, Clarendon Press, Oxford, 1999.
- [39] M.Yu. Lavrentiev, S.L. Dudarev, D. Nguyen-Manh, Magnetic cluster expansion simulations of FeCr alloys, *J. Nucl. Mater.* 386–388 (2009) 22–25.
- [40] H.A. Bethe, W.L. Bragg, Statistical theory of superlattices, *Proc. R. Soc. Lond. Ser. A Math. Phys. Eng. Sci.* 150 (871) (1935) 552–575.
- [41] E.A. Guggenheim, R.H. Fowler, Statistical thermodynamics of mixtures with zero energies of mixing, *Proc. R. Soc. Lond. Ser. A Math. Phys. Eng. Sci.* 183 (993) (1944) 203–212.
- [42] M.Yu. Lavrentiev, D. Nguyen-Manh, S.L. Dudarev, Magnetic cluster expansion model for bcc-fcc transitions in Fe and Fe-Cr alloys, *Phys. Rev. B* 81 (2010) 184202.
- [43] N. Saunders, A.P. Miodownik, CALPHAD (Calculation of Phase Diagrams): A Comprehensive Guide, Vol. 1, Pergamon, 1998.
- [44] B. Sundman, N. Dupin, B. Hallstedt, Algorithms useful for calculating multi-component equilibria, phase diagrams and other kinds of diagrams, *CALPHAD* 75 (2021) 102330.
- [45] J.O. Andersson, T. Helander, L. Höglund, P. Shi, B. Sundman, Thermo-Calc & DICTRA, computational tools for materials science, *CALPHAD* 26 (2) (2002) 273–312.
- [46] W. Cao, S.-L. Chen, F. Zhang, K. Wu, Y. Yang, Y.A. Chang, R. Schmid-Fetzer, W.A. Oates, PANDAT software with PanEngine, PanOptimizer and PanPrecipitation for multi-component phase diagram calculation and materials property simulation, *CALPHAD* 33 (2) (2009) 328–342.
- [47] A. van de Walle, R. Sun, Q.-J. Hong, S. Kadkhodaei, CALPHAD : Computer coupling of phase diagrams and software tools for high-throughput CALPHAD from first-principles data, *CALPHAD* 58 (2017) 70–81.
- [48] A.T. Dinsdale, SGTE data for elements, *CALPHAD* 15 (4) (1991) 317–425.
- [49] I. Toda-Caraballo, J.S. Wróbel, S.L. Dudarev, D. Nguyen-Manh, P.E.J. Rivera-Díaz-del Castillo, Interatomic spacing distribution in multicomponent alloys, *Acta Mater.* 97 (2015) 156–169.
- [50] G. Kresse, J. Hafner, Ab initio molecular dynamics for liquid metals, *Phys. Rev. B* 47 (1) (1993) 558–561.
- [51] G. Kresse, J. Hafner, Ab initio molecular-dynamics simulation of the liquid-metal-amorphous-semiconductor transition in germanium, *Phys. Rev. B* 49 (20) (1994) 14251–14269.
- [52] G. Kresse, J. Furthmüller, Efficiency of Ab-initio total energy calculations for metals and semiconductors using a plane-wave basis set, *Comput. Mater. Sci.* 6 (1) (1996) 15–50.
- [53] G. Kresse, J. Furthmüller, Efficient iterative schemes for Ab initio total-energy calculations using a plane-wave basis set, *Phys. Rev. B* 54 (16) (1996) 11169–11186.
- [54] P.E. Blöchl, Projector augmented-wave method, *Phys. Rev. B* 50 (24) (1994) 17953–17979.
- [55] G. Kresse, D. Joubert, From ultrasoft pseudopotentials to the projector augmented-wave method, *Phys. Rev. B* 59 (3) (1999) 1758–1775.
- [56] J.P. Perdew, K. Burke, M. Ernzerhof, Generalized gradient approximation made simple, *Phys. Rev. Lett.* 77 (18) (1996) 3865–3868.
- [57] J.D. Pack, H.J. Monkhorst, Special points for Brillouin-zone integrations, *Phys. Rev. B* 13 (12) (1976) 5188–5192.
- [58] A. van de Walle, G. Ceder, Automating first-principles phase diagram calculations, *J. Phase Equilib.* 23 (4) (2002) 348–359.
- [59] A. van de Walle, M. Asta, Self-driven lattice-model Monte Carlo simulations of alloy thermodynamic properties and phase diagrams, *Model. Simul. Mater. Sci. Eng. A* 10 (5) (2002) 521–538.
- [60] G.L.W. Hart, R.W. Forcade, Algorithm for generating derivative structures, *Phys. Rev. B* 77 (22) (2008) 224115.
- [61] D. Nguyen-Manh, M.Yu. Lavrentiev, S.L. Dudarev, Magnetic origin of nano-clustering and point defect interaction in Fe–Cr alloys: an Ab-initio study, *J. Comput. Aided Mater. Des.* 14 (2008) 159–169.
- [62] P. Erhart, B. Sadigh, A. Caro, Are there stable long-range ordered Fe_{1-x}Cr_x compounds? *Appl. Phys. Lett.* 92 (14) (2008) 141904.
- [63] L. Zhang, Y. Du, H. Xu, S. Liu, Y. Liu, F. Zheng, N. Dupin, H. Zhou, C. Tang, Phase equilibria and thermal analysis in the Fe–Mn–Ni system, *Int. J. Mater. Res.* 100 (2) (2009) 160–175.
- [64] A. Fernández-Caballero, M. Fedorov, J.S. Wróbel, P.M. Mummery, D. Nguyen-Manh, Configurational entropy in multicomponent alloys: Matrix formulation from Ab initio based hamiltonian and application to the FCC Cr-Fe-Mn-Ni system, *Entropy* 21 (1) (2019).
- [65] M. Fedorov, J.S. Wróbel, D. Nguyen-Manh, Fcc phase percentage in Cr-Fe-Mn-Ni alloys, *Mendeley Data V2* (2022).
- [66] M. Ferry, Direct Strip Casting of Metals and Alloys, Woodhead Publishing Limited, Cambridge, 2006.
- [67] L.I. Shvedov, Z.D. Pavlenko, Sigma-phase in the Fe-Cr-Mn-alloys, in: *Vestsi Akademii Navuk BSSR. Seryya Fizika-Tekhnichnykh Navuk*, 1975, pp. 14–17.
- [68] Y. Murata, K. Koyama, Y. Matsumoto, M. Morinaga, N. Yukawa, Equilibrium phase diagram of Fe-Cr-Mn ternary system, *ISIJ Int.* 80 (1990) 927–936.
- [69] E.K. Pickering, R. Muñoz-Moreno, H.J. Stone, N.G. Jones, Precipitation in the equiatomic high-entropy alloy CrMnFeCoNi, *Scr. Mater.* 113 (2016) 106–109.
- [70] K.A. Christofidou, T.P. McAuliffe, P.M. Mignanelli, H.J. Stone, N.G. Jones, On the prediction and the formation of the sigma phase in CrMnCoFeNi high entropy alloys, *J. Alloys Compd.* 770 (2019) 285–293.
- [71] H. Li, J. Ruan, N. Ueshima, K. Oikawa, Investigation on the sigma phase related equilibrium in Cr-Mn-Co system, *J. Alloys Compd.* 867 (2021) 159024.
- [72] D.P. Shoemaker, B.G. Bergman, The crystal structure of a sigma phase, FeCr, *J. Am. Chem. Soc.* 72 (1950) 5793.
- [73] N.Y. Samoylova, I.A. Bobrikov, E.A. Korneeva, R.N. Vasin, A.M. Balagurov, I.S. Golovin, Kinetic of the isothermal A2 to sigma phase transformation in Fe-Cr alloy, *J. Alloys Compd.* 913 (2022) 165282.